

Magnetic order of Dy³⁺ and Fe³⁺ moments in antiferromagnetic DyFeO₃ probed by spin Hall magnetoresistance and spin Seebeck effect

G. R. Hoogeboom¹, T. Kuschel², G.E.W. Bauer^{1,3}, M. V. Mostovoy¹, A. V. Kimel⁴ and B. J. van Wees¹

¹ *Physics of Nanodevices, Zernike Institute for Advanced Materials, University of Groningen, Nijenborgh 4, 9747 AG Groningen, The Netherlands.*

² *Center for Spinelectronic Materials and Devices, Department of Physics, Bielefeld University, Universitätsstraße 25, 33615 Bielefeld, Germany.*

³ *AIMR & Institute for Materials Research, Tohoku University, Aoba-ku, Katahira 2-1-1, Sendai, Japan*

⁴ *Spectroscopy of Solids and Interfaces, Institute of Molecules and Materials, Radboud University Nijmegen, Heyendaalseweg 135, 6525 AJ Nijmegen, The Netherlands*

(Dated: December 22, 2020)

We report on spin Hall magnetoresistance (SMR) and spin Seebeck effect (SSE) in single crystal of the rare-earth antiferromagnet DyFeO₃ with a thin Pt film contact. The angular shape and symmetry of the SMR at elevated temperatures reflect the antiferromagnetic order of the Fe³⁺ moments as governed by the Zeeman energy, the magnetocrystalline anisotropy and the Dzyaloshinskii-Moriya interaction. We interpret the observed linear dependence of the signal on the magnetic field strength as evidence for field-induced order of the Dy³⁺ moments up to room temperature. At and below the Morin temperature of 50 K, the SMR monitors the spin-reorientation phase transition of Fe³⁺ spins. Below 23 K, additional features emerge that persist below 4 K, the ordering temperature of the Dy³⁺ magnetic sublattice. We conclude that the combination of SMR and SSE is a simple and efficient tool to study spin reorientation phase transitions and sublattice magnetizations.

I. INTRODUCTION

Antiferromagnets (AFMs) form an abundant class of materials that offer many advantages over ferromagnets (FMs) for applications in high-density magnetic logics and data storage devices. AFMs support high-frequency dynamics in the THz regime that allows faster writing of magnetic bits compared to FMs. The absence of magnetic stray fields minimizes on-chip cross-talk and allows downsizing devices that are robust against magnetic perturbations [1]. On the other hand, most magnetic detection methods observe only the FM order. Recent developments in the detection [2] and manipulation [3–5] of the AFM order reveal its many opportunities.

The AFM DyFeO₃ (DFO) belongs to a family of rare-earth transition metal oxides called orthoferrites that display many unusual phenomena such as weak ferromagnetism (WFM), spin-reorientation transitions, strong magnetostriction, multiferroicity including a large linear magnetoelectric effect [6]. Their magnetic properties are governed by the spin and orbital momenta of 4f rare-earth ions coupled to the magnetic moment of 3d transition metal ions.

The magnetization of dielectrics can be detected electrically by the spin Hall magnetoresistance (SMR) in heavy metal contacts with a large spin Hall angle such as Pt [7]. This phenomenon is sensitive to FM, but also AFM spin order [2, 8–10]. With a Pt contact, information about AFMs can be also retrieved by the spin Seebeck effect (SSE) under a temperature gradient [11–13].

Here, we track the field-dependence of the coupled Dy³⁺ and Fe³⁺ magnetic order as a function of tem-

perature by both SMR and SSE. A sufficiently strong magnetic field in the *ab* plane of DFO forces the Néel vector to follow a complex path out of the *ab* plane. A theoretical spin model explains the observations in terms of Fe³⁺ spin rotations that are governed by the competition between the magnetic anisotropy, Zeeman energy, and Dzyaloshinskii-Moriya interaction (DMI). The Dy³⁺ moments are disordered at room temperature but nevertheless affect the magnitude of the SMR. At the so-called Morin phase transition at ~ 50 K the Fe³⁺ spins rotate by 90°, causing a step-like anomaly in the SMR. At even lower temperatures, we observe two separate features tentatively assigned to the re-orientation of Fe³⁺ spins in an applied magnetic field and another related to the ordering of Dy³⁺ orbital moments. Below 23 K, the SMR signal is $\sim 1\%$, 1-2 orders of magnitude larger than reported for other materials [2, 7]. Both Fe³⁺ and Dy³⁺ moments appear to contribute to the SSE; a magnetic field orders the Dy³⁺ moments and suppresses the Fe³⁺ contribution. The complex SMR and SSE is evidence of a coupling between the Fe³⁺ and Dy³⁺ magnetic subsystems.

The paper is organized as follows. In Section II we review the magnetic and multiferroic properties of DFO. The theory of the magnetic probing methods are discussed in Sec. III with Subsec. III A the SMR and Subsec. III B the SSE. In Subsec. IV A, the fabrication, characterization and measurement techniques are explained. Further, a model including the DMI, Zeeman energy and magnetic anisotropy is employed in Subsec. IV B. The SMR results at elevated temperatures including the model fits as well as SMR and SSE results at low

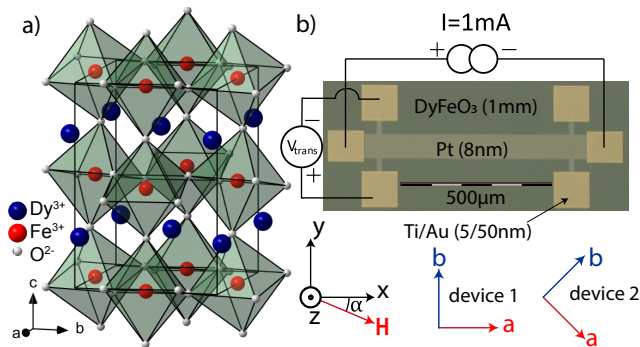


FIG. 1. (a) DFO crystal unit cell. The blue, red and white spheres represent Dy^{3+} , Fe^{3+} and O^{2-} ions, respectively. (b) Optical image of the Pt Hall bar on top of the bulk DFO crystal. The lines indicate voltage probes, AC source and angle α of the external magnetic field \mathbf{H} . In the two devices, the crystallographic directions a and b are rotated by 45° in the xy plane, the reference frame of the Hall bar.

temperatures are described and discussed in Sec. V.

II. MAGNETIC AND MULTIFERROIC PROPERTIES OF DFO

DFO is a perovskite with an orthorhombic (D_{2h}^{16} - Pbnm) crystallographic structure. It consists of alternating Fe^{3+} and Dy^{3+} ab planes, in which the Fe ions are located inside O^{2-} octahedrons (Fig. 1a)). The large Dy^{3+} magnetic moments ($J = 15/2$) order at a low temperature, $T_N^{\text{Dy}} = 4\text{K}$. The high Néel temperature $T_N^{\text{Fe}} = 645\text{K}$ indicates strong inter- and intra-plane AFM Heisenberg superexchange between the Fe^{3+} magnetic moments ($S = 5/2$). The AFM order of the Fe moments is of the G-type with Néel vector \mathbf{G} (anti)parallel to the crystallographic a axis (Γ_4 symmetry [14]). The broken inversion symmetry enables a DMI [15, 16] that in the Γ_4 -phase causes a WFM $\mathbf{m}_{\text{WFM}} \parallel \mathbf{c}$ by the small ($\sim 0.5^\circ$) canting of the Fe spins [14].

A first-order Morin transition from the WFM Γ_4 -phase to the purely AFM Γ_1 -phase occurs when lowering the temperature below 50 K. At this transition, the direction of the magnetic easy axis abruptly changes from the a - to the b -direction. A magnetic field higher than a critical magnetic field, H_{cr} , along the c axis re-orientates the Néel vector back to the a axis and recovers the Γ_4 -phase. Below T_N^{Dy} , the Dy^{3+} moments form a noncollinear Ising-like AFM order with Ising axes rotated by $\pm 33^\circ$ from the b axis [17] that corresponds to a $G'_a A'_b$ state in Bertaut's notation [18]. The simultaneous presence of ordered Fe and Dy magnetic moments breaks inversion symmetry and, under an applied magnetic field, induces an electric polarization [19] by exchange striction that couples the Fe and Dy magnetic sublattices [6, 20]. Higher magnetic fields destroy the AFM order of the Dy^{3+} moments and thereby the electric polarization [21].

Spins in this material can be controlled by light through the inverse Faraday effect [3], as well as by temperature and magnetic field. Re-orientation of the Fe moments has been studied by magnetometry [22], Faraday rotation [23], Mössbauer spectroscopy [24] and neutron scattering measurements [21]. The Morin transition at 50 K causes large changes in the specific heat [25] and entropy [26].

III. PROBING METHODS

A. Spin Hall magnetoresistance

The SMR is caused by the spin-charge conversion in a thin heavy metal layer in contact with a magnet [27]. The spin Hall effect induces a spin current transverse to an applied charge current and thereby an electron spin accumulation at surfaces and interfaces. Upon reflection at the interface to a magnetic insulator, electrons experience an exchange interaction that depends on the angle between their spin polarization and that of the interface magnetic moments, while the latter can be controlled by an applied magnetic field. The reflected spin current is transformed back into an observable charge current by the inverse spin Hall effect. The interface exchange interaction is parameterized by the complex spin mixing conductance. The result is a modulation of the charge transport that depends on the orientation of the applied current and the interface magnetic order. In a Hall bar geometry, this affects the longitudinal resistance and causes a planar Hall effect, i.e. a Hall voltage even when the magnetic field lies in the transport plane.

SMR is a powerful tool to investigate the magnetic ordering at the interface of collinear [7, 27–29] and non-collinear ferrimagnets [30, 31] as well as spin spirals [32, 33]. Recently, a “negative” SMR has been discovered for AFMs [2, 8–10], i.e. an SMR with a 90° phase shift of the angular dependence as compared to FMs, which shows that the AFM Néel vector \mathbf{G} tends to align itself normal to the applied magnetic field. The observable in AFMs is therefore the Néel vector rather than the net magnetization [2].

The longitudinal and transverse electrical resistivities ρ_L and ρ_T of Pt on an AFM read [2]

$$\rho_L = \rho + \Delta\rho_0 + \Delta\rho_1(1 - G_y^2) \quad (1)$$

$$\rho_T = \Delta\rho_1 G_x G_y + \Delta\rho_2 m_z + \Delta\rho_{\text{Hall}} H_z \quad (2)$$

with G_i and H_i with $i \in \{x, y, z\}$ as the Cartesian components of the (unit) Néel and the applied magnetic field vectors, respectively. m_z is the out-of-plane (OOP) component of the unit vector in the direction of the WFM magnetization. $\Delta\rho_0$ is an angle-independent interface correction to the bulk resistivity ρ . $\Delta\rho_{\text{Hall}} H_z$ is the ordinary Hall resistivity of Pt in the presence of an OOP component of the magnetic field. $\Delta\rho_1$ ($\Delta\rho_2$) is proportional

to the real (imaginary) part of the interface spin-mixing conductance. $\Delta\rho_2$ is a resistance induced by the effective WFM field, believed to be small in most circumstances.

The interface Dy^{3+} moments can contribute to the SMR when ordered. Below T_N^{Dy} , the Dy^{3+} moments are AFM aligned with Néel vector \mathbf{G}^{Dy} . Above T_N^{Dy} and in sufficiently large applied magnetic fields, the Dy^{3+} moments contribute to the SMR in Eqs. (1,2) after replacing the Néel vector \mathbf{G}^{Dy} by the (nearly perpendicular) magnetization \mathbf{m}^{Dy} . Disregarding magnetic anisotropy and DMI for the moment, the spin mixing conductance term $\Delta\rho_1 m_x^{\text{Dy}} m_y^{\text{Dy}}$ phase-shifts the SMR by 90° relative to the pure AFM contribution. The term $\Delta\rho_2 m_z$ changes sign with m_z and its contribution $\sim H_z$ cannot be distinguished from the ordinary Hall effect $\Delta\rho_{\text{Hall}} H_z$ in Pt. We remove a linear magnetic field dependence from the OOP SMR measurements. Residual non-linear effects from $\Delta\rho_2 m_z$ may persist, but should be small in the Γ_4 phase. A finite $\Delta\rho_2 m_z$ has been reported in conducting AFMs [34], but we do not observe a significant contribution down to 60 K.

B. Spin Seebeck effect

A heat current in a FM excites a spin current that in insulators is carried mainly by magnons, the quanta of the spin wave excitations of the magnetic order. We can generate a temperature bias simply by the Joule heating of a charge current in a metal contact. A magnon flow \mathbf{j}_m can also be generated by a gradient of a magnon accumulation or chemical potential μ_m [35]. Therefore

$$\mathbf{j}_m = -\sigma_m(\nabla\mu_m + S_S\nabla T) \quad (3)$$

with σ_m as the magnon spin conductivity and S_S the spin Seebeck coefficient. Thermal magnons can typically diffuse over several μm [36–38], which implies that the SSE mainly probes bulk rather than interface magnetic properties. The magnons in simple AFMs typically come in degenerate pairs with opposite polarization that split under an applied magnetic field [11, 39]. The associated imbalance of the magnon populations cause a non-zero spin Seebeck effect [13]. Paramagnets display a field-induced SSE effect [38] for the same reason, so aligned Dy^{3+} moments can contribute to an SSE in DFO. A magnon accumulation at the interface to Pt injects a spin current \mathbf{j}_s that can be observed as an inverse spin Hall effect voltage $\mathbf{V}_{\text{ISHE}} = \rho\theta_{\text{SH}}(\mathbf{j}_s \times \boldsymbol{\sigma})$, where θ_{SH} is the spin Hall angle and $\boldsymbol{\sigma}$ is the spin polarization. The SMR and SSE can be measured simultaneously by a lock-in technique [40].

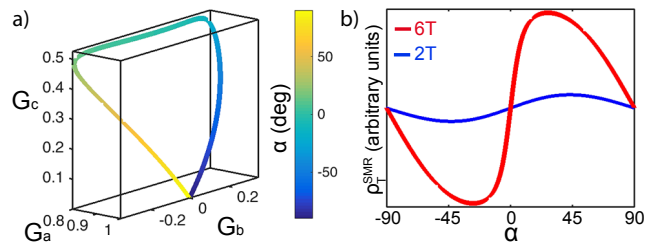


FIG. 2. Néel vector, $\mathbf{G} = (G_a, G_b, G_c)$ with $|\mathbf{G}| = 1$, calculated as a function of the magnetic field in the ab plane. The angle $\alpha \in [-90^\circ, 90^\circ]$ as defined in Fig. 1(b) is coded by the colored bar. $\mathbf{G}(\alpha)$ minimizes the free energy Eq. (4), for $K_b = 0.15$ K per Fe ion and $H = 6$ T (other parameters are given in the text). (b) The transverse SMR (arbitrary units) due to the magnetic Fe sublattice for $H = 6$ T, i.e. the $\mathbf{G}(\alpha)$ from panel (a) (thick red line), and for $H = 2$ T (thin blue line).

IV. METHODS

A. Fabrication, characterization and measurements

We confirmed the crystallographic direction of our single crystal by X-ray diffraction before sawing it into slices along the ab plane and polishing them. Two devices were fabricated on different slices of the materials using a three step electron beam lithography process; markers were created to align the devices along two different crystallographic directions. After fabrication of an 8 nm thick Pt Hall bar, 50 nm Ti/Au contact pads were deposited.

The angular dependence of the magnetoresistance below 50 K is complex and hysteretic. Phase changes are associated by internal strains that can cause cracks in the bulk crystal. We therefore carried out magnetic field sweeps at low temperatures very slowly, with a waiting time of 60 seconds between each field step. The response was measured with a 1 mA (100 μA) AC current through the Pt Hall bar in device 1 (device 2) with a frequency of 7.777 Hz. The first and second harmonic transverse and longitudinal lock-in voltages as measured with a superconducting magnet in a cryostat with variable temperature insert are the SMR and SSE effects, respectively.

Below the transition temperature, the Morin transition is induced by a magnetic field along the c axis that rotates the Néel vector from \mathbf{a} to \mathbf{b} . For device 1, this does not change the transverse resistance since $G_x^{\text{Fe}} G_y^{\text{Fe}} = 0$ when the Néel vector is in either the x - or y -direction. On the other hand, device 2 is optimized for the observation of the Morin transition, because, as discussed below, the transverse resistance should be maximally positive when $\mathbf{G} \parallel \mathbf{b}$ and maximally negative when $\mathbf{G} \parallel \mathbf{a}$.

B. Modelling the SMR of Pt|DFO

The orientation of the Néel vector \mathbf{G} of the Fe sublattice at temperatures well above T_N^{Dy} is governed by several competing interactions: (a) the magnetic anisotropy, which above the Morin transition favors $\mathbf{G}\|\mathbf{a}$, (b) the Zeeman energy that favors $\mathbf{G} \perp \mathbf{H}$ since the transverse magnetic susceptibility of an AFM is higher than the longitudinal one, and (c) the coupling of the WFM moment, $\mathbf{m}_{\text{WFM}}\|\mathbf{a}$, to the applied magnetic field. This competition can be described phenomenologically by the free energy density

$$f = \frac{K_b}{2}G_b^2 + \frac{K_c}{2}G_c^2 + \frac{\chi_{\perp}}{2}[(\mathbf{G} \cdot \mathbf{H})^2 - \mathbf{H}^2] - m_{\text{WFM}}G_cH_a, \quad (4)$$

with the first two terms describing the second-order magnetic anisotropy with magnetic easy, intermediate and hard axes along the a , b and c crystallographic directions, respectively ($K_c > K_b > K_a = 0$), χ_{\perp} is the transverse magnetic susceptibility, and the m_{WFM} is the weak ferromagnetic moment along the a axis, induced by $\mathbf{G}\|\mathbf{c}$. $|\mathbf{G}| = 1$, because the longitudinal susceptibility of the Fe spins is very small for $T \ll T_N^{\text{Fe}}$. The magnetic field \mathbf{H} is chosen parallel to the ab plane, but \mathbf{G} can have an OOP component $G_c \neq 0$ since the third term in Eq.(4) couples G_c linearly to H_a . For the SMR at 250 K, we may disregard higher-order magnetic anisotropies that become important near the Morin transition.

At weak magnetic fields, the magnetic anisotropy pins the Néel vector to the a axis. When the Zeeman energy becomes comparable with the anisotropy energy, the rotation of the magnetic field vector in the ab plane gives rise to a concomitant rotation of \mathbf{G} . In the absence of magnetic anisotropy, the canting of the magnetic moments leads to $\mathbf{G} \perp \mathbf{H}$ for any magnetic field orientation due to the Zeeman energy rendering a sinusoidal SMR, but magnetic anisotropy can distort the angular dependence. This behavior is further complicated by the WFM: for strong magnetic fields along the a axis, the Néel vector tilts away from the ab plane towards the c axis, since the c -component of \mathbf{G} induces a WFM moment parallel to the applied magnetic field [24, 41]. By contrast, G_b does not give rise to a weak FM moment, so the Néel vector returns into the ab plane when we rotate the magnetic field away from the a axis. The equilibrium Néel vector minimizes the free energy Eq. (4) under the constraint $|\mathbf{G}| = 1$ as a function of strength and orientation of the magnetic field with in-plane (IP) angle α (see Fig. 1b)).

We adopt a weak magnetization parameters $m_{\text{WFM}} = 0.133 \mu_B$ per Fe^{3+} ion induced either by $\mathbf{G}\|\mathbf{c}$ along the a axis [42] or by $\mathbf{G}\|\mathbf{a}$ along the c axis [43]. The transverse magnetic susceptibility can be estimated using the Heisenberg model with an Fe-Fe exchange constant $J_1 = 4.23 \text{ meV}$ for $\text{Y}_3\text{Fe}_5\text{O}_{12}$ [44], which leads to $\chi_{\perp} = \mu_B^2 / (3J_1)$, which does not depend strongly on the rare-earth ion. K_c governs the critical field when applied along the a axis with $\mu_0 H_{\text{cr}} = 9.3 \text{ T}$ at $T = 270 \text{ K}$ [24] that

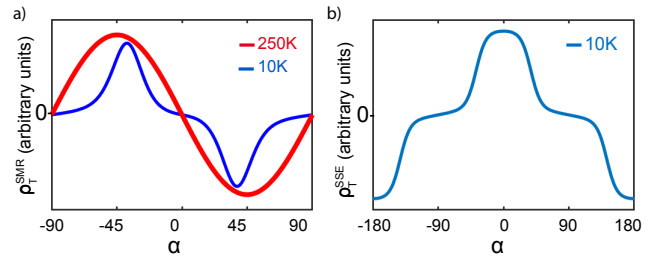


FIG. 3. Calculated angular dependence of the transverse a) SMR (ρ_T^{SMR}) and b) local SSE (ρ_T^{SSE}) as contributed by paramagnetic Dy^{3+} moments polarized by an applied field $H = 6 \text{ T}$. The curve at 10 K (blue line) is calculated numerically using Eq. 5. The 250 K curve (amplified by a factor 100, red line) is obtained analytically from Eq. (6). Both SMR and SSE grow with decreasing temperature and associated increasing Dy^{3+} magnetization.

fully rotates \mathbf{G} from the a to the c direction. K_c can then be estimated using $K_c = m_{\text{WFM}}H_{\text{cr}} + \chi_{\perp}H_{\text{cr}}^2$. K_b is the only free temperature-dependent parameter that we fit to the field-dependent SMR. All other constants are taken to be independent of temperature. A typical calculated dependence of $\mathbf{G}(\alpha)$ and the corresponding contribution of the Fe spins to the SMR is shown in Fig. 2 (see below for a more detailed discussion).

Ordered rare-earth ions can also contribute to the SMR and SSE. The spectrum of the lowest-energy ${}^6\text{H}_{15/2}$ multiplet of the Dy^{3+} ion ($4f^9$ electronic configuration) consists of a Kramers doublet separated by $\Delta = 52 \text{ cm}^{-1}$ ($\approx 75 \text{ K}$) from the first excited state [45]. At low temperatures, $k_B T \ll \Delta$, the Dy moments behave as Ising spins tilted by an angle $\pm\phi_{\text{Dy}}$ away from the a axis in the ab plane ($\phi_{\text{Dy}} = 57^\circ$). At high temperatures, $k_B T \gg \Delta$, they can be described as anisotropic Heisenberg spins with paramagnetic susceptibilities, $\chi_{\parallel}^{\text{Dy}}(\chi_{\perp}^{\text{Dy}})$ for a magnetic field parallel (perpendicular) to the local spin-quantization axis ($\chi_{\parallel}^{\text{Dy}} > \chi_{\perp}^{\text{Dy}}$) [46].

For $k_B T \gg \Delta$, the SMR resulting from the contributions of the four Dy sublattices (four Dy sites in the crystallographic unit cell of DFO) is

$$R_T^{\text{SMR}} \propto -A[H^2 \sin(2\alpha) - 2Hg_1G_c \sin \alpha] - 2BHg_2G_c \sin \alpha, \quad (5)$$

where the first term originates from the interaction of Dy spins with the applied magnetic field and the other two terms result from the exchange field induced by Fe spins on Dy sites (for a more detailed discussion of the effective magnetic field acting on Dy spins and the expressions for A and B in terms of the magnetic susceptibilities of the Dy ions see Appendix B). It can be inferred from Fig. 2a) that G_c is approximately proportional to $\cos \alpha$. Therefore, all terms in Eq. 5 give the $\sin(2\alpha)$ dependence of the transverse SMR at high temperatures (thick red line in Fig. 3 a)). Equation (5) should be added to the SMR caused by the iron sublattice with an unknown

weight that is governed by the mixing conductance of the Dy sublattice. We may conclude however that an additional $\sin(2\alpha)$ should not strongly change the shape of the SMR in Figure 2b).

At low temperatures, $T \ll \Delta/k_B$, the Dy moments behave as Ising spins. A rotation of the magnetic field in the ab plane modulates the projection of the effective magnetic field on the local spin-quantization axes of the four Dy sublattices, which affects the angular dependence of the SMR. Since the paramagnetic model Eq. (5) cannot be used anymore, we compute the Dy contribution to the SMR $\sim m_x m_y$ numerically for the rare-earth Hamiltonian

$$H_{Dy}^{(i)} = g_J \mu_B (\mathbf{J} \cdot \mathbf{H}_{Dy}) - \frac{K}{2} (\mathbf{J} \cdot \hat{\mathbf{z}}_i)^2, \quad i = 1, 2, 3, 4, \quad (6)$$

with \mathbf{J} as the Dy total angular momentum, $g_J = 4/3$ the Landé factor, $K = \Delta/7$ the anisotropy parameter, which is known to reasonably describe the low-energy excited states of Dy ions and $\hat{\mathbf{z}}_i$ are the local easy axes rotated by $+57^\circ$, for the Dy sublattices 1 and 3, and -57° , for the sublattices 2 and 4, away from the a axis. The magnetic field \mathbf{H}_{Dy} acting on Dy spins is the sum of the applied field and the exchange field from Fe spins: $\mathbf{H}_{ex} = g_1 G_z \hat{\mathbf{a}} \pm g_2 G_z \hat{\mathbf{b}}$, where the \pm is for the sublattices 1, 3 and 2, 4, respectively. We neglect the c component of the exchange field, since the Dy magnetic moment along the c is small and does not affect the SMR. Using the Hamiltonian Eq. (6), we calculate the average a and b components of the magnetic moments of the 4 Dy sublattices at a temperature T and the resulting contributions to SMR. The angular dependence of the SMR due to Dy spins is plotted in Fig. 3 a).

The calculations recover the $\sin(2\alpha)$ angular dependence of the SMR from Eq.(5) at high temperatures. At 10 K (blue line) the SMR curve becomes strongly deformed: The angular dependence of the SMR shows peaks and dips at the effective field directions orthogonal to the quantization axis $\hat{\mathbf{z}}_i$ of the i -th rare-earth sublattice.

For long magnon relaxation time, the SSE generated a spin current that is assumed to be proportional to the bulk magnetization and can therefore provide additional information. We focus here on the low temperature regime because we did not observe an SSE at elevated temperature, which is an indication that the Dy magnetization plays an important role.

A net magnetization of rare-earth moments affects the SSE signals in gadolinium iron [47] and gadolinium gallium [38] garnets. We assume that the SSE is dominated by a spin current from the bulk that is proportional to the total magnetization \mathbf{m}_b^{Dy} of the four Dy sublattices that we calculated for the Hamiltonian Eq. (6) at 10 K as function of the angle α of the applied magnetic field. The model predicts peaks at magnetic field directions aligned with the Ising-spin axes of the Dy moments, i.e. in between those canted by $\pm 33^\circ$, which enhances the magnetization. The contribution from the Fe sublattice to

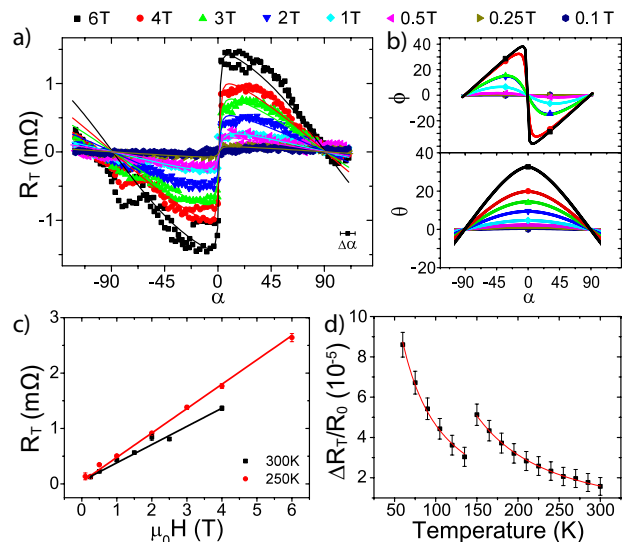


FIG. 4. (a) Transverse SMR (symbols) measured as a function of IP magnetic field angle α and strength (indicated at the top). The measurements are done on device 1 with a current of 1 mA at 250 K and the error bar $\Delta\alpha$ indicates a systematic error due to a possible misalignment of the magnetic field direction as compared to the crystallographic axes. The lines are fits obtained by adjusting K_b in the free energy model Eq. (4). (b) The IP (ϕ) and OOP (θ) canting angles of the Néel vector with respect to \mathbf{b} as a function of the IP magnetic field direction from the fits. (c) The maximal signal change $\Delta R_{T,r}$ during a magnetic field rotation depends linearly on the magnetic field strength and (d) shows a power-law temperature dependence, $\Delta R_{T,r}/R_0 \propto (T)^\epsilon$. R_0 is the sheet resistance obtained from the base resistance of the corresponding longitudinal measurements adjusted by the geometrical factor length/width of the Hall bar. These measurements are carried out at 4 T.

the SSE is expected to depend as $\cos \alpha$ on the external magnetic field direction [48]. The ratio of the Fe and Dy contributions to SSE is unknown.

V. RESULTS

The SMR was measured by rotating an IP magnetic field of various strengths. Temperature drift and noise swamped the small signal in the longitudinal resistance as discussed in Appendix A. Figure 4 a) shows the measured resistance of device 1 at 250 K in the transverse (planar Hall) configuration using the left contacts in Fig. 1 b). The results for the right Hall contacts (not shown) are very similar.

The (negative) sign of the SMR agrees with our Fe sublattice model, suggesting that it is caused by the AFM ordered Fe spins with Néel vector \mathbf{G} normal to the applied magnetic field. However, \mathbf{G} cannot be strictly normal to the magnetic field, because the SMR is not proportional to $\sin(2\alpha)$, as observed for example in NiO [2]. The strongly non-sinusoidal angular dependence of the SMR

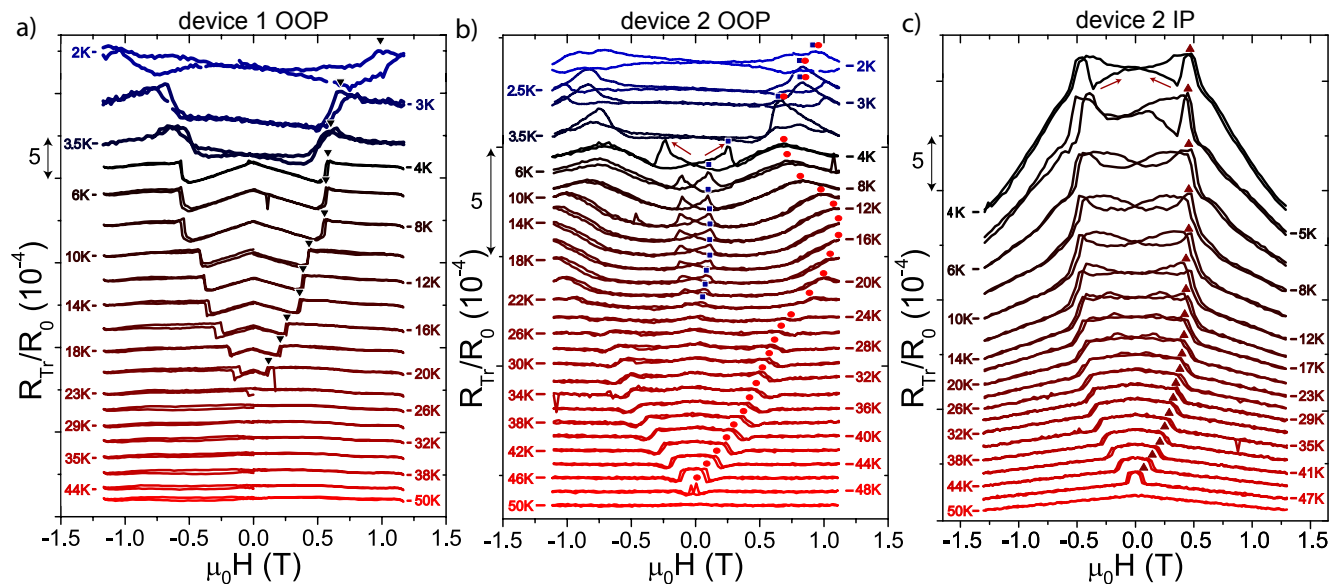


FIG. 5. The relative changes in the transverse resistances R_{Tr}/R_0 of (a) devices 1 and (b,c) device 2. A linear contribution from the ordinary Hall effect has been subtracted from the OOP data. Offsets of the order of 10^{-4} are removed and the curves are shifted with respect to each other for clarity. The magnetic field directions are (a,b) along \mathbf{z} for the OOP and (c) along \mathbf{y} for the IP configurations. (a) The data for device 1 are expected to not change during the Morin transition. The observed SMR is symmetric with respect to current and magnetic field reversal and sensitive to Dy^{3+} ordering. (b,c) Device 2 reveals the Morin transition by a positive step for weak magnetic fields. Below 23 K, hysteretic resistance features emerge when sweeping the fields back and forth that vanishes at higher magnetic fields and temperatures. The arrows indicate the magnetic field sweep directions, while the symbols highlight the critical magnetic fields as summarized in Fig. 6.

is evidence for a non-trivial path traced by the Néel vector in an applied magnetic field as predicted by the model Eq. (4).

Figure 2 a) shows the dependence of the three components G_a , G_b and G_c of the Néel vector on the IP orientation angle α of the magnetic field, for $\mu_0 H = 6$ T. The value of $\alpha \in [-90^\circ, 90^\circ]$ is indicated by the color code side bar. When $\alpha = 0$ ($\mathbf{H} \parallel \mathbf{a}$), the magnetic field causes a tilt of \mathbf{G} away from the easy a axis towards the hard c axis since the Néel vector parallel to the c axis induces a magnetization along the a axis. The excursion of \mathbf{G} from the ab plane effectively reduces the role of the IP magnetic anisotropy, which leads to a large rotation of the Néel vector in the ab plane for small α (at nearly constant G_c). As explained above, this rotation is driven by the Zeeman energy of the AFM ordered Fe spins (the third term in Eq.(4)), which favors $\mathbf{G} \perp \mathbf{H}$ and competes with the magnetic anisotropy that favors $\mathbf{G} \parallel \mathbf{a}$ (the first term in Eq.(4)). This behavior is similar to the spin-flop transition for a magnetic field applied along the magnetic easy axis, except that \mathbf{G} does not become fully orthogonal to the magnetic field. As the magnetic field vector rotates away from the a axis, G_c and $|G_b|$ decrease, and at $\alpha = \pm 90^\circ$, \mathbf{G} is parallel to the a axis.

The sensitivity of \mathbf{G} to small α gives rise to an abrupt change of the transverse SMR that is proportional to $G_a G_b$ close to $\alpha = 0$ (thick red line Fig. 2b). The calculated and observed SMR scans agree well for $T = 250$ K and $\mu_0 H = 6$ T. Surprisingly, the shape of the experi-

mental curves is practically the same at all magnetic field strengths, i.e. the SMR jumps at $\alpha = 0$ even at weak fields, while the calculation approach the geometrical $\sin(2\alpha)$ dependence (thin blue line in Fig. 2b) calculated for $\mu_0 H = 2$ T). The fits of the observed SMR for all magnetic fields require a strongly field-dependent IP anisotropy parameter K_b that is very small in the zero field limit: $K_b = (6 \pm 8) \cdot 10^{-6} + (3.20 \pm 0.02) \cdot 10^{-3} (H/T)^2$ K (see Fig. 4a). At present we cannot explain this behavior. The Dy^{3+} moments should not play an important role in this regime unless a Pt induced anisotropy at the DFO/Pt interface modifies their magnetism (see below).

The exchange coupling between the rare-earth and transition-metal magnetic subsystems is reflected by the second term in Eq.(5) of the Dy^{3+} contribution to the SMR that is proportional to G_c , i.e. the AFM order of the Fe spins. Since, G_c is a smooth function at $\alpha = 0$, it cannot be hold responsible for the large zero-field magnetoresistance. The angular SMR appears to be dominated by the Néel vector \mathbf{G} of the Fe moments, in contrast to SmFeO_3 , in which the Sm-ions determine not only the amplitude but also the sign of the SMR [49].

The linear increase of the SMR with magnetic field strength (see Fig. 4c)) can partly be explained by the growth of the maximum IP rotation angle, ϕ , of the Néel vector with magnetic field. However, deviations from the linear dependence are then expected close to the critical value, $H_a \sim 9$ T, at which the re-orientation transition from $\mathbf{G} \parallel \mathbf{a}$ to $\mathbf{G} \parallel \mathbf{c}$ in $\mathbf{H} \parallel \mathbf{a}$ is complete [24]. Nevertheless,

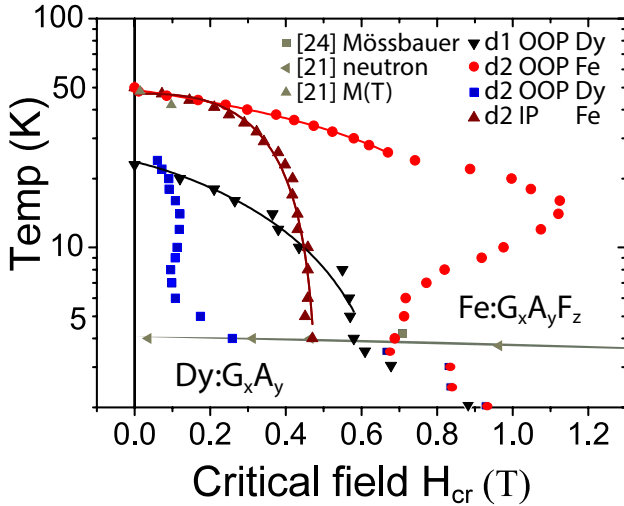


FIG. 6. Critical magnetic fields H_{cr} of the observed transitions in the transverse resistance as a function of temperature. Symbols correspond to Fig. 5, where they denote the step functions that trace the Morin transition in device 2. \blacktriangle indicates IP and \bullet OOP magnetic field directions. The latter symbol describes the peaks at lower temperatures as well. The OOP H_{cr} of the low magnetic field features are shown for device 1 (\blacktriangledown) and device 2 (\blacksquare). The features for the IP magnetic field directions are less pronounced and not shown. The lines show a fit by the function $H_c \propto (T_M - T)^\epsilon$, which is used to extract the ordering temperatures of 50 K and 23 K for the Morin transition and a magnetic phase transition to an ordered Dy^{3+} sublattice, respectively. Further data is from Refs. [21, 24], obtained by Mössbauer spectrometry (\blacksquare), neutron scattering (\blacktriangleleft) and magnetometry (\blacktriangle).

the SMR signal shows no sign of saturation at $\mu_0 H_a = 6$ T and $T = 250$ K. The $\mu_0 H$ of Dy becomes of the order of $k_B T$ at a magnetic field strength of 37 T, indicating contributions from the paramagnetic rare earth spins remains linear in the applied field strengths.

Further evidence for rare earth contributions at higher temperatures is the Curie-like power-law temperature dependence of the SMR (see Fig. 4d)) $\text{SMR} \sim T^\epsilon$, with $\epsilon = -1.24 \pm 0.04$ at low temperatures and $\epsilon = -1.67 \pm 0.02$ at high temperatures.[50] For comparison, in the AFM NiO, ϵ is positive and the SMR signal grows quadratically with the AFM order parameter [2]. At temperatures well below the Néel transition $T_N^{\text{Fe}} = 645$ K, the Fe based magnetic order is nearly temperature independent. The strong magnetic field and temperature dependence therefore suggest important contributions from polarized Dy^{3+} moments even at room temperature.

The puzzling strong magnetic field-dependence of K_b from the data fit might indicate a different coupling between the rare earth and transition metal magnetic subsystems at the interface and in the bulk. It can be justified by the following symmetry argument. The generators of the Pbnm space group of the DFO crystal are three (glide) mirror planes: \tilde{m}_a , \tilde{m}_b and m_c , i.e. a mirror reflection combined with a shift along a direction parallel

to the mirror plane. m_c is broken at the interface normal to the c axis. In the absence of m_c , the rare earth order parameters A'_a and G'_b transform to G_b that describes the AFM order of Fe spins, which allows for a linear coupling between the rare earth and Fe spins at the interface. Since G_b strongly depends on α at $\alpha = 0$, the same may hold for the rare earth moments at the interface. The SMR is very surface sensitive and could be strongly affected by this coupling.

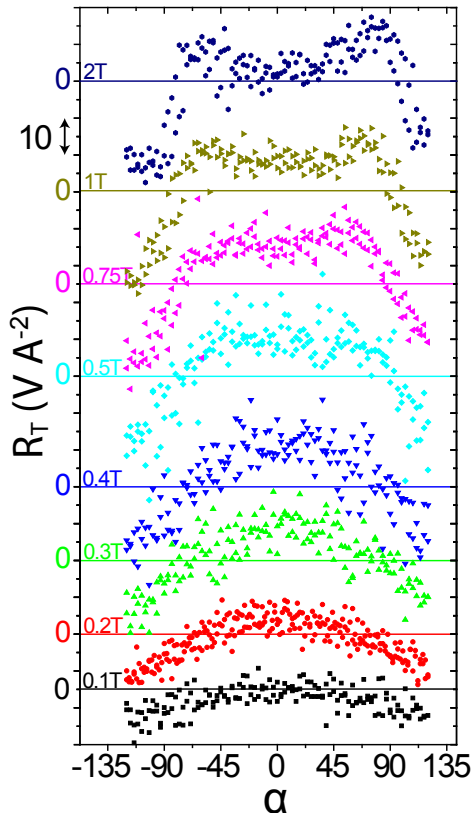
Next, we turn to the SMR at temperatures below the Morin transition at magnetic fields around the re-entrant field, H_{cr} . Figure 5(a) shows the transverse SMR of device 1 in an OOP magnetic field, while the data for longitudinal resistance are deferred to the Appendix A, Fig. 8a). We subtracted a linear field dependent contribution from the OOP data that is caused by the ordinary Hall effect in Pt.

The zero-field resistance of device 1 should not change under the Morin transition when the Néel vector direction switches from a to b nor should it be affected by weak magnetic fields $\mathbf{H} \parallel c$ ($\mu_0 H_{cr} < 0.1$ T near 50 K [21]) that return the system to $\mathbf{G} \parallel a$. Indeed, we do not see any weak-field anomaly of the SMR near 50 K in Fig. 5a). However, below 23 K, a negative SMR proportional to the applied field appears. The linear field-dependence ends abruptly with a positive step-like discontinuity (see Fig. 5a)). No resistance offset has been observed between the zero-field Γ_1 and the high-field Γ_4 phases. After subtraction of the strictly linear ordinary Hall effect contribution, the SMR feature is an even function of H_c . The magnetic phase transition at 23 K appears to be unrelated to the Morin transition and has not been reported previously.

The Morin transition is clearly observed in the OOP and IP SMR of device 2, in which the crystallographic axes are azimuthally rotated by 45° relative to the Hall bar as shown in Fig. 1b). Here, an SMR signal is expected for both magnetic phases and the 90° rotation of the Néel vector from a to b should change its sign from positive for the AFM Γ_1 phase ($\mathbf{G} \parallel \mathbf{b}$) to negative for the WFM Γ_4 phase ($\mathbf{G} \parallel \mathbf{a}$), for $|H_c| > H_{cr}$. The Γ_1 phase can also be suppressed by an IP field $\mathbf{H} \parallel \hat{y} = \hat{b} - \hat{a}$ that rotates the Néel vector towards \hat{b} to lower the Zeeman energy. The drop in the Hall resistance observed in device 2 below 48 K for the OOP (Fig. 5 b)) and IP (Fig. 5 c)) field directions can therefore be ascribed to the Morin transition with a temperature-dependent H_{cr} . The SMR steps are negative, as expected.

At even lower temperatures the model appears to break down since we observe hysteretic behavior in the field-dependence of the SMR signal at low magnetic fields for both the OOP and IP directions. These features come up below 23 K, so appear to have the same origin as the anomalies in device 1. For the OOP direction, the low-field anomalies in device 2 are peaks while they are step-like in device 1. Wang et al.[21] did not observe a hysteresis in the Fe^{3+} magnetic sublattice and suggested that observed hysteretic behaviour [6, 51] is an evidence

FIG. 7. The SSE, i.e. the detected voltage in the transverse Hall probe divided by the squared current of device 1 at 10 K as a function of the magnetic field strength and direction α . At weak fields, the SSE shows a $\cos \alpha$ dependence as expected for the Fe^{3+} magnetic sublattice. This amplitude initially increases with the magnetic field strength but decreases again and flattens for $H > 0.5$ T.



for long-range to short-range Dy^{3+} magnetic order. The SMR might witness an ordering of Dy^{3+} moments at the interface at a higher temperature than in the bulk that cannot be detected by other measurements.

Another unexpected feature is a linear negative magnetoresistance at $|H_y| > H_{\text{cr}}$ for the IP configuration (see Fig. 5c) that might be caused by a canting of \mathbf{G}^{Fe} towards \mathbf{c} by $H_a > 1.6$ T [24]. A misalignment of the crystallographic axes could also affect the SMR more significantly for high magnetic fields. However, neither of these mechanisms explain the IP magnetic field dependence and the peaks and low magnetic field features in the OOP measurements of both devices below 23 K (Fig. 5a) and 5b)). Since their signs and shapes vary, we can exclude a paramagnetic OOP canting of the Dy^{3+} orbital moments. The Dy^{3+} orbital moments are locked to the Ising axis in the ab plane and the magnetization is one order of magnitude larger in this plane than along the c direction [6]. This might explain the IP SMR features in terms of an IP field and temperature dependent order of the Dy^{3+} moments.

The 90° spin reorientation at the Morin transition maximizes the Fe^{3+} contribution to the SMR. The in-

crease of the IP signal amplitude by one order of magnitude upon lowering the temperature, see Fig. 5(c) is therefore unexpected. The signals become as large as 1%, one order of magnitude larger than the SMR signals of Pt on $\text{Y}_3\text{Fe}_5\text{O}_{12}$ [7, 27–29] and a factor four larger than that of $\alpha\text{-Fe}_2\text{O}_3$ [52]. Ordered Dy^{3+} magnetic moments appear to be responsible for the anomalous signals below 23 K. They interact with the Fe sublattice by the exchange interaction, as observed before in the multiferroic phase at temperatures exceeding T_N^{Dy} under a 0.5 T magnetic field [21]. A contribution of Dy^{3+} moments to the magnetization has also been observed in terms of an upturn of the magnetization and hyperfine field below 23 K [53].

The SMR steps in device 1 around $T_N^{\text{Dy}} = 4$ K at which the Dy moments order spontaneously, are similar to those at higher temperature, which supports the hypothesis that the latter are also related to Dy^{3+} order. Device 2 shows an increased H_{cr} matching those in device 1 at these temperatures. Both devices show no non-linear antisymmetric field dependence, indicating that the Dy^{3+} ordering above 4 K is field-induced. Li et al. [51] observed jumps in the thermal conductivity around 4 T and attributed these to a spin reorientation of the Fe sublattice. However, no further transitions are observed up to 6 T as is shown in Appendix A, so we cannot confirm such an Fe^{3+} transition.

The magnetic field and temperature of the occurrences of SMR steps at spin transitions and of SMR anomalies are collected in Fig. 6, including the peaks in the OOP measurements of device 2, using the same markers as in Fig. 5. The data on the Morin transition agrees with previous observations [21, 24]. The Morin point for both IP an OOP configurations is around 50 K, whereas the transitions ascribed to an ordering of the Dy^{3+} moments occur around 23 K. Upon lowering the temperature, the transitions associated to the Dy^{3+} and Fe^{3+} moments approach each other and merge below T_N^{Dy} , which is another indication of a strong inter-sublattice exchange interaction.

Figure 7 summarizes the observed IP SSE data of device 1 at 10 K. The angular dependence of the resistance at small fields shows the $\cos \alpha$ dependence, indicating that the magnon spin current \mathbf{j}_m injected into Pt is constant with angle. The amplitude initially increases linearly with field, but decreases again for $H > 0.5$ T. The SSE signal of a uniaxial AFM has $\cos \alpha$ dependence for an IP rotating magnetic field [48]. The SSE is small at angles for which our model for the Dy^{3+} contribution in Fig. 3b) predicts a peak. However, we do not observe the expected Dy^{3+} -induced SSE contribution due to the Dy^{3+} magnetization shown in Fig. 3. On the contrary, an increase in Dy^{3+} magnetization appears to suppress the SSE signal. These results suggest that the angular dependence of the SSE is governed not so much by the ordering of the Dy spins, but by their effect on the frequencies of the antiferromagnons in the Fe magnetic subsystem. The ordering of Dy spins leads to a hardening

of the AFM resonance modes [54]. The applied magnetic field suppresses the Dy spin ordering and results in a substantial decrease of the spin gap [54], which affects the thermal magnon flux and, hence, the SSE. At room temperature, the SSE signal does not rise above the noise level of 0.18 V A^{-2} .

VI. CONCLUSION

We studied the rare earth ferrite DFO by measuring the transverse electric resistance in Pt film contacts as function of temperature and applied magnetic field strength and direction. Results are interpreted in terms of SMR and SSE for magnetic configurations that minimize a magnetic free energy model with magnetic anisotropies, Zeeman energy and DMI. The Néel vector appears to slowly rotate OOP and displays jumps under IP rotating magnetic fields. Magnetic field-strength dependences indicate that Fe^{3+} spins are responsible for the symmetry of the SMR, but that the Dy^{3+} orbital moments affect the amplitude. The first-order Morin transition is clearly observed at temperatures below 50 K. Additional sharp features emerge below 23 K at critical fields below that of the Morin transition. These observed features cannot be understood by the Fe^{3+} Néel vector driven SMR. Rather, they suggest a magnetic field-

induced ordering of Dy^{3+} established by the competition between applied magnetic and exchange fields with Fe^{3+} . This hypothesis is supported by the similar SMR features at the spontaneous Dy^{3+} moment ordering temperature T_N^{Dy} . A Dy^{3+} order above T_N^{Dy} also appears to suppress the SSE contributions from the Fe sublattice.

Concluding, we report simultaneous manipulation and monitoring of the ordering of both transition metal and rare earth magnetic sublattices and their interactions as a function of temperature and magnetic field in the complex magnetic material DFO.

VII. ACKNOWLEDGEMENTS

We thank A. Wu for growing the single crystal DyFeO_3 , J. G. Holstein, H. Adema, T. J. Schouten, H. H. de Vries and H. M. de Roos for their technical assistance as well as R. Mikhaylovskiy and A. K. Zvezdin for discussions. This work is part of the research program Magnon Spintronics (MSP) No. 159 financed by the Nederlandse Organisatie voor Wetenschappelijk Onderzoek (NWO) and JSPS KAKENHI Grant Nos. 19H006450, and the DFG Priority Programme 1538 Spin-Caloric Transport (KU 3271/1-1). Further, the Spinoza Prize awarded in 2016 to B. J. van Wees by NWO is gratefully acknowledged

-
- [1] S. Loth, S. Baumann, C. P. Lutz, D. M. Eigler, and A. J. Heinrich, *Science* **335**, 196 (2012).
 - [2] G. R. Hoogeboom, A. Aqeel, T. Kuschel, T. T. M. Palstra, and B. J. van Wees, *Applied Physics Letters* **111**, 052409 (2017).
 - [3] D. Afanasiev, B. A. Ivanov, A. Kirilyuk, T. Rasing, R. V. Pisarev, and A. V. Kimel, *Physical Review Letters* **116**, 097401 (2016).
 - [4] P. Wadley, B. Howells, J. Železný, C. Andrews, V. Hills, R. P. Campion, V. Novák, K. Olejník, F. Maccherozzi, S. S. Dhesi, S. Y. Martin, T. Wagner, J. Wunderlich, F. Freimuth, Y. Mokrousov, J. Kuneš, J. S. Chauhan, M. J. Grzybowski, A. W. Rushforth, K. Edmond, B. L. Gallagher, and T. Jungwirth, *Science* **351**, 587 (2016).
 - [5] T. Moriyama, K. Oda, T. Ohkochi, M. Kimata, and T. Ono, *Scientific reports* **8**, 14167 (2018).
 - [6] Y. Tokunaga, S. Iguchi, T. Arima, and Y. Tokura, *Physical Review Letters* **101**, 097205 (2008).
 - [7] H. Nakayama, M. Althammer, Y. T. Chen, K. Uchida, Y. Kajiwara, D. Kikuchi, T. Ohtani, S. Geprägs, M. Opel, S. Takahashi, R. Gross, G. E. W. Bauer, S. T. B. Goennenwein, and E. Saitoh, *Physical Review Letters* **110**, 206601 (2013).
 - [8] J. Fischer, O. Gomonay, R. Schlitz, K. Ganzhorn, N. Vlietstra, M. Althammer, H. Huebl, M. Opel, R. Gross, S. T. B. Goennenwein, and S. Geprägs, *Physical Review B* **97**, 014417 (2018).
 - [9] Y. Ji, J. Miao, Y. M. Zhu, K. K. Meng, X. G. Xu, J. K. Chen, Y. Wu, and Y. Jiang, *Appl. Phys. Lett.* **112**, 232404 (2018).
 - [10] R. Lebrun, A. Ross, O. Gomonay, S. Bender, L. Baldrati, F. Kronast, A. Qaiumzadeh, J. Sinova, A. Brataas, R. Duine, and M. Kläui, *Communications Physics* **2**, 50 (2019).
 - [11] S. M. Wu, W. Zhang, A. Kc, P. Borisov, J. E. Pearson, J. S. Jiang, D. Letterman, A. Hoffmann, and A. Bhattacharya, *Physical Review Letters* **116**, 097204 (2016).
 - [12] S. M. Rezende and J. B. S. Mendes, *Applied Physics Letters* **111**, 172405 (2017).
 - [13] G. R. Hoogeboom and B. J. van Wees, *Physical Review B* **102**, 214415 (2020).
 - [14] E. A. Turov, *Physical Properties of Magnetically Ordered Crystals* (Izd. Akad. Nauk SSSR, 1963).
 - [15] I. Dzyaloshinsky, *J. Phys. Chem. Solids* **5**, 253 (1958).
 - [16] T. Moriya, *Physical Review* **120**, 91 (1960).
 - [17] L. M. Holmes, L. G. Van Uitert, R. R. Hecker, and G. W. Hull, *Physical Review B* **5**, 138 (1972).
 - [18] E. F. Bertaut, “Spin Configurations of Ionic Structures: Theory and Practice.” (1963).
 - [19] T. Yamaguchi and K. Tsushima, *Physical Review B* **8**, 5187 (1973).
 - [20] A. Stroppa, M. Marsman, G. Kresse, and S. Picozzi, *New Journal of Physics* **12**, 093026 (2010).
 - [21] J. Wang, J. Liu, J. Sheng, W. Luo, F. Ye, Z. Zhao, X. Sun, S. A. Danilkin, G. Deng, and W. Bao, *Physical Review B* **93**, 140403(R) (2016).
 - [22] P. Belov, A. K. Zvezdin, M. Kadomtseva, and I. B. Krynetskii, *Journal of Experimental and Theoretical*

- Physics **40**, 980 (1974).
- [23] A. Maziewski and R. Szymczak, *Journal of Physics D: Applied Physics* **10**, 37 (1977).
- [24] L. A. Prelorendjo, C. E. Johnson, M. F. Thomas, and B. M. Wanklyn, *Journal of Physics C: Solid State Physics* **13**, 2567 (1980).
- [25] F. Zhang, S. Li, J. Song, J. Shi, and X. Sun, *IEEE Transactions on Magnetics* **51**, 1000904 (2015).
- [26] Y. J. Ke, X. Q. Zhang, H. Ge, Y. Ma, and Z. H. Cheng, *Chinese Physics B* **24**, 037501 (2015).
- [27] Y. T. Chen, S. Takahashi, H. Nakayama, M. Althammer, S. Goennenwein, E. Saitoh, and G. Bauer, *Physical Review B* **87**, 144411 (2013).
- [28] N. Vlietstra, J. Shan, V. Castel, J. Ben Youssef, G. E. W. Bauer, and B. J. van Wees, *Applied Physics Letters* **103**, 032401 (2013).
- [29] M. Althammer, S. Meyer, H. Nakayama, M. Schreier, S. Altmannshofer, M. Weiler, H. Huebl, S. Geprägs, M. Opel, R. Gross, D. Meier, C. Klewe, T. Kuschel, J. M. Schmalhorst, G. Reiss, L. Shen, A. Gupta, Y. T. Chen, G. E. W. Bauer, E. Saitoh, and S. T. B. Goennenwein, *Physical Review B* **87**, 224401 (2013).
- [30] K. Ganzhorn, J. Barker, R. Schlitz, B. A. Piot, K. Ollefs, F. Guillou, F. Wilhelm, A. Rogalev, M. Opel, M. Althammer, S. Geprägs, H. Huebl, R. Gross, G. E. W. Bauer, and S. T. B. Goennenwein, *Physical Review B* **94**, 094401 (2016).
- [31] B. W. Dong, J. Cramer, K. Ganzhorn, H. Y. Yuan, E. J. Guo, S. Goennenwein, and M. Kläui, *Journal of Physics: Condensed Matter* **30**, 035802 (2018).
- [32] A. Aqeel, N. Vlietstra, J. A. Heuver, G. E. Bauer, B. Noheda, B. J. Van Wees, and T. T. Palstra, *Physical Review B* **92**, 224410 (2015).
- [33] A. Aqeel, N. Vlietstra, A. Roy, M. Mostovoy, B. J. Van Wees, and T. T. Palstra, *Physical Review B* **94**, 1334418 (2016).
- [34] K. Zhao, T. Hajiri, H. Chen, R. Miki, H. Asano, and P. Gegenwart, *Physical Review B* **100**, 45109 (2019).
- [35] L. J. Cornelissen and B. J. Van Wees, *Physical Review B* **93**, 020403 (2016).
- [36] L. J. Cornelissen, J. Liu, R. A. Duine, J. b. Youssef, and B. J. Van Wees, *Nature Physics* **11**, 1022 (2015).
- [37] R. Lebrun, A. Ross, S. A. Bender, A. Qaiumzadeh, L. Baldrati, J. Cramer, A. Brataas, R. A. Duine, and M. Kläui, *Nature* **561**, 222 (2018).
- [38] K. Oyanagi, S. Takahashi, L. J. Cornelissen, J. Shan, S. Daimon, T. Kikkawa, G. Bauer, B. J. van Wees, and E. Saitoh, *Nature Communications* **10**, 4740 (2019).
- [39] R. Cheng, J. Xiao, Q. Niu, and A. Brataas, *Physical Review Letters* **113**, 057601 (2014).
- [40] N. Vlietstra, J. Shan, B. J. van Wees, M. Isasa, F. Casanova, and J. B. Youssef, *Physical Review B* **90**, 174436 (2014).
- [41] V. V. Eremenko, S. L. Gnatchenko, N. F. Kharchenko, P. P. Lebedev, K. Piotrowski, H. Szymczak, and R. Szymczak, *Europhysics Letters* **11**, 1327 (1987).
- [42] S. Cao, L. Chen, W. Zhao, K. Xu, G. Wang, Y. Yang, B. Kang, H. Zhao, P. Chen, A. Stroppa, R. Zheng, J. Zhang, W. Ren, J. Íñiguez, and L. Bellaiche, *Scientific Reports* **6**, 37529 (2016).
- [43] A. K. Zvezdin, V. M. Matveev, A. A. Mukhin, and A. I. Popov, *Moscow, Izd. Nauk*, 296 (1985).
- [44] C. Hahn, G. de Loubens, V. V. Naletov, J. B. Youssef, O. Klein, and M. Viret, *European Physics Letters* **108**, 571 (2014).
- [45] A. K. Zvezdin and V. M. Matveev, *Zh. Eksp. Teor. Fiz., Tech. Rep.* 3 (1979).
- [46] U. V. Valiev, J. B. Gruber, S. A. Rakhimov, and O. A. Nabelkin, *physica status solidi (b)* **237**, 564 (2003).
- [47] S. Geprägs, A. Kehlberger, F. Coletta, Z. Qiu, E. J. Guo, T. Schulz, C. Mix, S. Meyer, A. Kamra, M. Althammer, H. Huebl, G. Jakob, Y. Ohnuma, H. Adachi, J. Barker, S. Maekawa, G. E. W. Bauer, E. Saitoh, R. Gross, S. T. B. Goennenwein, and M. Kläui, *Nature Communications* **7**, 10452 (2016).
- [48] W. Yuan, Q. Zhu, T. Su, Y. Yao, W. Xing, Y. Chen, Y. Ma, X. Lin, J. Shi, R. Shindou, X. C. Xie, and W. Han, *Science Advances* **4**, 1098 (2018).
- [49] T. Hajiri, L. Baldrati, R. Lebrun, M. Filianina, A. Ross, N. Tanahashi, M. Kuroda, W. L. Gan, T. O. Mentes, F. Genuzio, A. Locatelli, H. Asano, and M. Kläui, *Journal of Physics: Condensed Matter* **31**, 445804 (2019).
- [50] We have not been able to identify the mechanism for the step observed between 135 K and 150 K that has to our knowledge not been reported elsewhere either.
- [51] Z. Y. Zhao, X. Zhao, H. D. Zhou, F. B. Zhang, Q. J. Li, C. Fan, X. F. Sun, and X. G. Li, *Physical Review B* **89**, 224405 (2014).
- [52] J. Fischer, M. Althammer, N. Vlietstra, H. Huebl, S. Goennenwein, R. Gross, S. Geprägs, and M. Opel, *Physical Review Applied* **13**, 014019 (2020).
- [53] S. S. K. Reddy, N. Raju, C. G. Reddy, P. Y. Reddy, K. R. Reddy, and V. R. Reddy, *Journal of Magnetism and Magnetic Materials* **396**, 214 (2015).
- [54] T. N. Stanislavchuk, Y. Wang, Y. Janssen, G. L. Carr, S. W. Cheong, and A. A. Sirenko, *Physical Review B* **93**, 094403 (2016).
- [55] S. L. Gnatchenko, K. Piotrowski, A. Szewczyk, R. Szymczak, and H. Szymczak, *Journal of Magnetism and Magnetic Materials* **129**, 307 (1994).
- [56] J. H. Han, C. Song, F. Li, Y. Y. Wang, G. Y. Wang, Q. H. Yang, and F. Pan, *Physical Review B* **90**, 144431 (2014).
- [57] K. Oyanagi, J. M. Gomez-Perez, X. Zhang, T. Kikkawa, Y. Chen, E. Sagasta, L. E. Hueso, V. N. Golovach, F. S. Bergeret, F. Casanova, and E. Saitoh, arXiv:2008.02446 (2020).

Appendix A: Longitudinal and 2K SMR

The modulation of the longitudinal Pt resistance as a function of magnetic field are shown in Fig. 8 for comparison with the transverse SMR. The longitudinal signals are affected by a background contact resistance that is sensitive to temperature changes. The SMR signals are therefore more distorted by a small temperature drift than the transverse measurements. Moreover, the background resistance suffer from increased noise.

The OOP resistance changes of device 1 are one order of magnitude larger than those of device 2 and dominated by hysteretic effects. The signal amplitudes of OOP and IP configurations for device 2 are similar. The measurement time of one data point below 0.2 T is smaller than at larger fields, influencing the shape of the graphs. Device 2 shows hysteretic features at low magnetic fields and be-

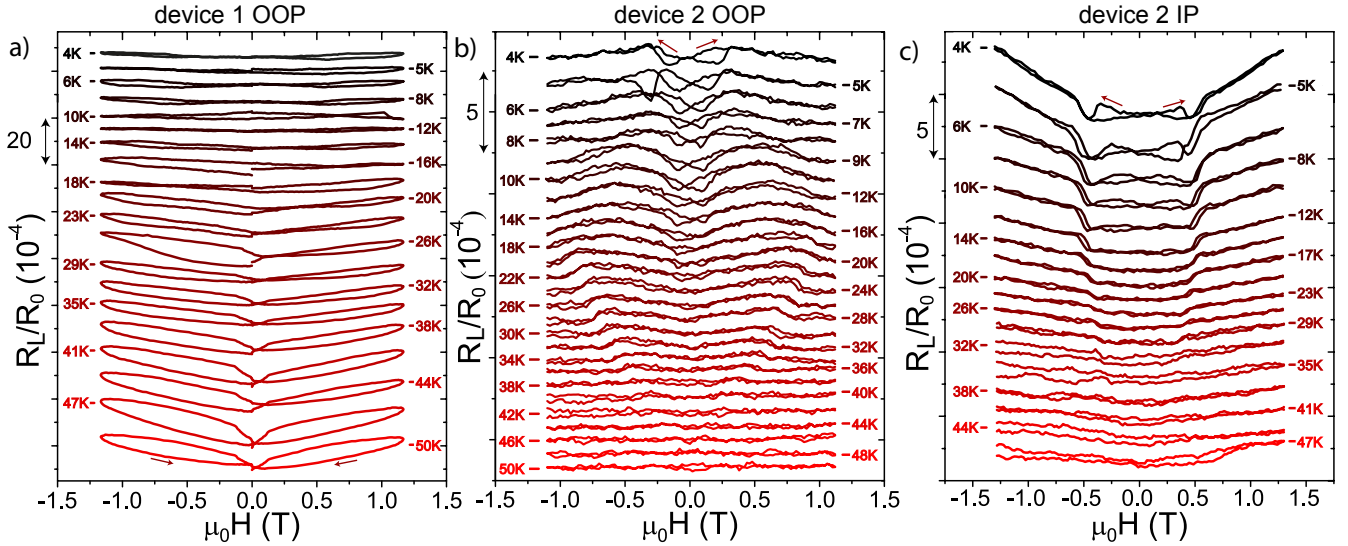


FIG. 8. Relative changes in the longitudinal SMR R_L/R_0 of (a) device 1 as well as (b,c) device 2 at temperatures up to 50K for magnetic field sweeps (a,b) OOP and (c) IP. Device 1 shows large hysteretic effects at the full range of magnetic field strengths. The amount of data points around zero magnetic field, and thus the waiting time per magnetic field change, is higher than at higher fields as to have higher resolution for the transverse Morin transition. This makes the hysteretic effects slightly distorted compared to a situation with constant waiting time. Device 2 shows hysteretic effects solely at lower field strengths which corresponds to the hysteretic features of the transverse measurements.

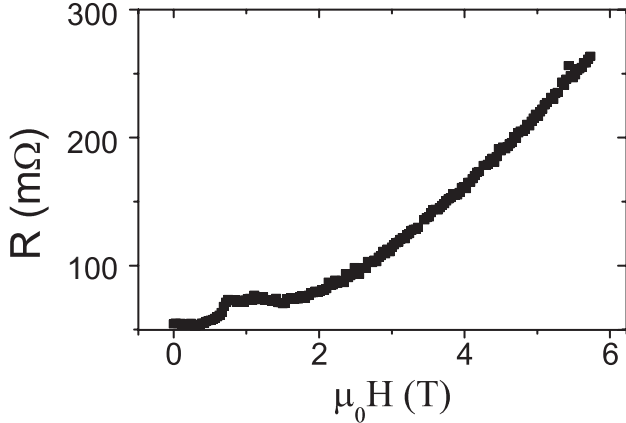


FIG. 9. Transverse resistance of device 2 at 2K as a function of the OOP magnetic field up to 6T. The resistance increases continuously with magnetic field strength above 2T.

low 23K, for both IP and OOP magnetic fields that are similar to the transverse SMR features discussed in the main text.

Results of a field sweep up to 6 T are shown in Fig. 9. The resulting continuous curve does not show transitions on top of those discussed in the text, without evidence for a phase transition at 4 T and 2 K [51, 55].

Appendix B: Exchange interaction

The $Pbnm$ crystal symmetry allows an exchange coupling between the Dy^{3+} moments and G-type AFM ordered Fe spins. The coupling of the 4 (individual) Dy spins in the unit cell with the Fe spins is described as

$$\begin{aligned}
 E_{Dy-Fe} = & -g_1 G_c (m_1^a + m_2^a + m_3^a + m_4^a) \\
 & -g_2 G_c (m_1^a - m_2^a + m_3^a - m_4^a) \\
 & -g_3 G_a (m_1^c + m_2^c + m_3^c + m_4^c) \\
 & -g_4 G_b (m_1^c - m_2^c + m_3^c - m_4^c), \quad (B1)
 \end{aligned}$$

where the indices 1, 2, 3, 4 label the rare-earth ions in the unit cell. The exchange field from Fe ions is estimated to be ~ 2 T at low temperatures [45].

For $k_B T \gg \Delta$, the magnetization of the Dy sublattice $m_{\parallel} = \chi_{\parallel}^{Dy} H_{\parallel}$ and $m_{\perp} = \chi_{\perp}^{Dy} H_{\perp}$ for field components parallel and perpendicular to the local anisotropy axis and $H = \sqrt{H_{\parallel}^2 + H_{\perp}^2}$. We assume that the transverse SMR caused by the paramagnetic Dy^{3+} moments polarized by the applied field is proportional to $m_x m_y$ [9, 32, 56, 57]. Adding the contributions of the four Dy sites in the crystallographic unit cell of DFO and the exchange field from the Fe spins acting on the Dy spins as described in the main text, we obtain Eq. 5 with $A = [(\chi_{\parallel}^{Dy} + \chi_{\perp}^{Dy})^2 - (\chi_{\parallel}^{Dy} - \chi_{\perp}^{Dy})^2 \cos(4\phi_{Dy})]/2$ and $B = \sin(2\phi_{Dy}) [(\chi_{\parallel}^{Dy})^2 - (\chi_{\perp}^{Dy})^2 - (\chi_{\parallel}^{Dy} - \chi_{\perp}^{Dy})^2 \cos(2\phi_{Dy})]$. The coupling constants g_3 and g_4 do not appear in the expression for SMR since the latter does not depend on the c-component of Dy spins. Moreover, the

c-component is very small at low temperatures, since the easy axes of Dy ions lie in the ab plane. Both g_1 and g_2 lead to (nearly) the same angular dependence of SMR.